applied sciences

MDPI

Article

Finite Element Analysis of Tyre Contact Interaction Considering Simplified Pavement with Different Aggregate Sizes

Zhi Li, Weiyong Chen, Yinghui Li and Wenliang Wu *

School of Civil Engineering and Transportation, South China University of Technology, Guangzhou 510640, China; lizhi@scut.edu.cn (Z.L.); 202121010428@mail.scut.edu.cn (W.C.); 202221010106@mail.scut.edu.cn (Y.L.)
* Correspondence: ctwlwu@scut.edu.cn

Abstract: This study considered the effect of pavement aggregate grain size on tyre–pavement contact interaction during the late stages of pavement skid resistance. First, hemispherical shells 7, 9, and 13 mm in diameter were used to simulate coarse pavement aggregates. Subsequently, a three-dimensional finite element tyre–pavement contact model developed using ABAQUS was employed to analyse the contact interaction between each simplified pavement type and the tyre under steady–state rolling and braking conditions. Finally, the concept of occlusal depth was proposed and applied to characterise pavement skid resistance. The results showed that under steady–state rolling conditions, the peak contact stress of the simplified pavement increased with the pavement mean texture depth, whereas the contact area decreased. Under steady–state braking conditions, the effect of the contact interaction between the tyre and simplified pavement aggregates was ranked in order of superiority as aggregate grain sizes of 9, 7, and 13 mm, indicating that aggregate grain size did not exhibit any correlation with tyre–pavement contact interaction. Additionally, the squares of linear correlation coefficients between the pavement cumulative occlusal depth and horizontal braking force reached 0.921, 0.941, 0.889, and 0.894 for vehicle speeds of 30, 60, 90, and 120 km/h, respectively, indicating that they could be used to assess pavement skid resistance.

Keywords: finite element model; aggregate grain size; tyre–pavement contact interaction; occlusal depth

check for updates

Citation: Li, Z.; Chen, W.; Li, Y.; Wu, W. Finite Element Analysis of Tyre Contact Interaction Considering Simplified Pavement with Different Aggregate Sizes. *Appl. Sci.* **2023**, *13*, 12011. https://doi.org/10.3390/app132112011

Academic Editors: Edgar Sokolovskij and Vidas Žuraulis

Received: 9 October 2023
Revised: 28 October 2023
Accepted: 31 October 2023
Published: 3 November 2023

1. Introduction

The skid resistance of an asphalt pavement is a critical factor affecting road traffic safety [1–3]. Whilst driving, vehicle tyres are in direct contact with the pavement; thus, tyre–pavement contact interaction is a crucial aspect determining asphalt pavement skid resistance. The primary factors affecting tyre–pavement interaction are the tyre characteristics (tyre tread, tyre pressure, driving speed, etc.), pavement characteristics (aggregate properties, aggregate grain size, pavement macrotexture, etc.), and external environment (temperature, water, snow, etc.) [4–6].

Many researchers have studied tyre–pavement contact interactions. Zhang et al. [7,8] used a pressure–sensitive, electrically conductive rubber sensor to measure the contact pressure between the tyre and pavement and successively analysed the corresponding tyre–pavement contact interaction under static and dynamic conditions; however, they ignored the effects of the tyre texture and pavement macrotexture. Chen et al. [9] measured the contact pressure between a tyre and pavements of different macrotextures under static conditions using a pressure film and showed that the pavement macrotexture and tyre load had a greater effect on tyre–pavement contact than the tyre inflation pressure; however, the study lacked a dynamic analysis of tyre–pavement contact.

Indoor testing is a vital research method; however, it can be easily affected by external factors and consumes considerable manpower and material resources. At the same time, tyre–pavement contact analysis involves complex nonlinear mechanical problems. With the rapid development of computers, finite element analysis allows for intuitive and accurate solutions to complex non-linear mechanical problems. Consequently, finite element numerical simulation has become a more effective means of studying tyre–pavement contact interactions. Liu and Al-Qadi [10,11] used a deep learning approach to predict 3D tyre–pavement contact stresses based on finite element generated tyre contact stress datasets and developed ContactNet and ContactGAN models for the fast prediction of 3D tyre pavement stresses. Xie and Yang [12], He et al. [13], and Tang et al. [14] used the ABAQUS finite element-based software package to develop a three-dimensional (3D) tyre–pavement contact model and analyse the impact of driving speed, tyre load, and tyre pressure on tyre–pavement contact interactions under different driving conditions; however, the pavement model applied during their study ignored the pavement macrotexture.

As road researchers, we would prefer to focus on the impacts of factors such as the pavement macrotexture and aggregate properties on tyre–pavement contact interaction. Lin and Wang [15] analysed the effect of fine-aggregate angularity (FAA) on asphalt pavement skid resistance using the British Pendulum Number test. The results showed that the pavement FAA had a considerable effect on skid resistance at the macrotexture level. Xiao et al. [16] analysed the contributions of different texture wavelengths on the aggregate surface to tyre–pavement interaction. The results showed that the correlation between textures with small-scale wavelengths and tyre–pavement interaction decreased with increasing sliding speed; the correlation changed in the opposite direction for textures with large-scale wavelengths. Riahi et al. [17] considered the interaction between the pavement macrotexture and tyre rolling process to propose a model based on the dissipation of energy by the rubber block during the cyclic deformation of the pavement in concave and convex cycles. Yu et al. [18] selected seven parameters to characterise pavement texture features and analysed the impact of those features on pavement skid resistance. Sharma et al. [19] developed a multi-physics tyre–pavement contact model based on the temperature and pavement texture, focusing on the impact of pavement macrotexture on tyre–pavement interaction. Finite element simulation technology can be applied to further analyse tyre–pavement contact interactions; however, in analysing the factors affecting tyre–pavement contact interactions, previous studies considered the tyre factors but ignored the effect of the pavement macrotexture and considered the effect of the aggregate surface properties but paid little attention to the effect of the aggregate grain size after the aggregate texture was abraded.

Consequently, this study focused on the impact of aggregate grain size on tyre–pavement contact interaction. Three groups of simplified pavements comprising single-diameter hemispherical shells were designed. A 3D tyre–pavement contact model developed using ABAQUS 2021 was subsequently employed to analyse the contact interaction between each simplified pavement and a tyre under steady–state rolling and braking conditions. Finally, we summarised the change law of the contact interaction between tyres and aggregates of different grain sizes in simplified pavements and proposed reasonable evaluation indices to guide the design of asphalt pavement skid resistance.

2. Contact Theory

During the normal vehicle driving process, tyre–pavement contact can be divided into three general regions, as shown in Figure 1. Region I denotes before contact (where the tyre and pavement are about to make contact); Region II denotes stable contact (where the tyre and pavement are in full contact); and Region III denotes after contact (where the tyre and pavement experience contact detachment). When the vehicle brakes, the impact force generated in contact Region I and the adhesion friction generated in contact Region III contribute less to the tyre's overall friction, and the vehicle's braking force comes from contact Region II. Consequently, this study focused on the contact behaviour in Region II (full contact state).

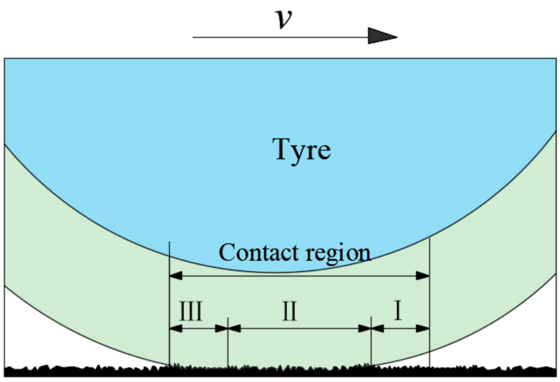

Figure 1. Schematic of the tyre–pavement contact region.

The contact behaviour in Region II primarily comprises tyre–pavement aggregate contact interaction. Because the tyre's internal inflatable structure and tread material stiffness are considerably lower than those of the pavement aggregate, the tyre produces a localised wrapping of the raised aggregate on the pavement during the rolling process. When the vehicle brakes, the speed of the outer edge of the tyre line is less than the vehicle's driving speed; consequently, the tyre and raised aggregate produce an "occlusal braking" effect. This effect can be explained by the hysteresis effect (F_h) of the aggregate as well as the adhesion (F_a) between the tread and pavement materials [20,21], as shown in Figure 2. The hysteresis effect is primarily a result of the resistance provided by the occlusion of the tread with the raised pavement aggregates and the surface friction generated by the relative slip between them. Because the adhesion interaction between materials has a small effect on the overall friction behaviour, its magnitude is negligible [22,23]. Consequently, this study ignored the effect of adhesion and focused on the contact interaction between the tyre and pavement aggregates.

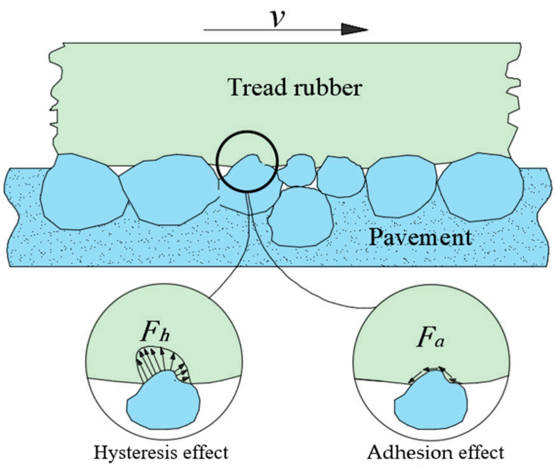

Figure 2. Analysis of tyre–pavement contact interaction.

Additionally, research and practice have shown that during the early stages of road use, different pavement types can provide excellent skid resistance, although their macrotextures vary considerably. With repeated traffic loads, pavement aggregate angles and surface microtextures are repeatedly abraded to present a smoother surface; therefore, the skid resistances of different pavements will exhibit different degrees of attenuation. However, pavement aggregate grain size is a critical factor affecting pavement macrotexture [24–26]. Consequently, attention must be paid to the effect of aggregate grain size on pavement skid resistance. To analyse the contact interaction between a tyre and aggregates of different grain sizes in this study, hemispherical shells were used to simulate abraded coarse aggregates, as shown in Figure 3.

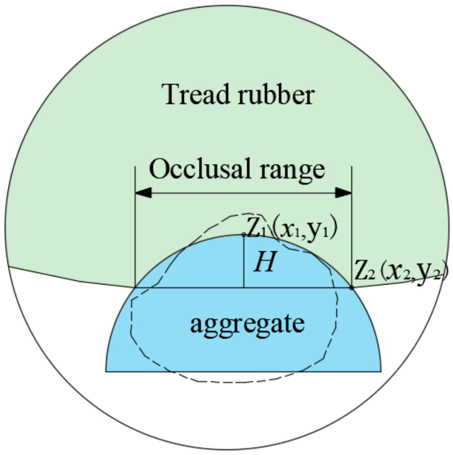

Figure 3. Schematic of occlusal depth using a hemispherical shell.

To model the local package behaviour produced by the process of rolling tyre deformation on pavement raised aggregates, this study proposed the concept of "occlusal depth", which refers to the package depth of a tyre on pavement raised aggregate. Within the occlusal range of the tyre and aggregate, the occlusal depth (H) of a single aggregate is expressed using the difference between the vertex elevation value of the aggregate ($Z_1(x_1, y_1)$) and the critical point elevation of the aggregate ($Z_2(x_2, y_2)$), as shown in Figure 3. It can be calculated as follows:

$$H = Z_1(x_1, y_1) - Z_2(x_2, y_2) \tag{1}$$

where H denotes the occlusal depth of a single aggregate, $Z_1(x_1, y_1)$ denotes the vertex elevation in the occlusal range, and $Z_2(x_2, y_2)$ denotes the critical point elevation in the occlusal range. The mean occlusal depth of the simplified pavement can be calculated as follows:

$$\overline{H} = \frac{\sum_{i=1}^{n} H_i}{n} \tag{2}$$

where $\overline{H}$ denotes the mean occlusal depth of the simplified pavement, $\sum_{i=1}^{n} H_i$ denotes the cumulative occlusal depth of the simplified pavement, and n denotes the number of aggregates in contact with the tyres.

We initially assumed that a greater degree of tyre tread deformation (larger occlusal depth) would result in better contact interaction between the tyre and pavement raised aggregate; this assumption was investigated using the 3D tyre–pavement contact finite element model presented in Section 4.

3. Methods: Finite Element Modelling

3.1. Tyre Model

3.1.1. Tyre Type and Material Parameters

The tyre type selected for this study was a 175/80 R14 radial tyre (where 175 denotes a tyre section width of 175 mm, 80 denotes an aspect ratio of 80%, R denotes a radial tyre type, and 14 denotes a nominal rim diameter of 14 in). A radial tyre is a complex composite comprising rubber and cord skeleton materials. The rubber material includes the tread rubber, crown rubber, and carcass rubber, and the cord skeleton material includes two belt cord layers and one carcass cord layer, as shown in Figure 4.

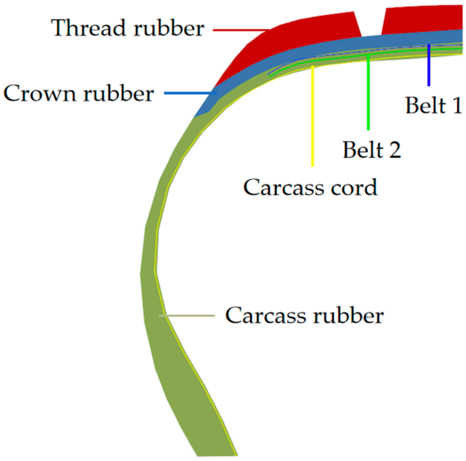

Figure 4. Material composition of the tyre.

The neo-Hookean and linear elasticity intrinsic models were used to numerically simulate the tyre rubber and cord skeleton materials, respectively. The strain energy function is expressed as follows:

$$U = C_{10}(\overline{I_1} - 3) + \frac{1}{D_1}(\overline{J_e} - 1)^2$$

where U denotes strain potential energy, C_{10} denotes the shear characteristics of the material, $\overline{J_e}$ denotes the elastic volume ratio, $\overline{I_1}$ denotes the deformation of the material, and D_1 denotes the compression characteristics of the material.

The tyre industry does not make the exact material properties and structural design of tyres available to the general public. At the same time, the workload and cost of testing for tyre materials are relatively large. Therefore, the mechanical parameters of these materials in Yu et al. [25] are used, as shown in Tables 1 and 2.

Table 1. Rubber material parameters for the 175/80 R14 radial tyre.

Material	Neo-Hookean Model		Density (g/cm^3)
	C_{10} (MPa)	D_1 (MPa^{-1})	
Tread rubber	0.835	0.024	1.12
Crown rubber	0.869	0.04	1.12
Carcass rubber	1.0	0.02	1.15

Table 2. Cord skeleton material parameters for the 175/80 R14 radial tyre.

Material	Cross-Sectional Area (mm^2)	Spacing (mm)	Angle (°)	Young's Modulus (10^5 MPa)	Poisson's Ratio	Density (g/cm^3)
Belt 1	0.212	1.16	70	1.722	0.3	5.9
Belt 2	0.212	1.16	110	1.722	0.3	5.9
Carcass cord	0.421	1.0	0	9.87	0.3	1.5

3.1.2. 2D and 3D Tyre Modelling

This study focused on the contact interaction between the rubber tread material and the different grain size aggregates when the tyre is running in the longitudinal direction; ignoring the transverse tyre tread pattern had little effect on the analysis results. Meanwhile, to save computational time, the tyre modelling ignored the transverse tyre tread pattern and retained only the two longitudinal grooves. As the work of tyre modelling is two-dimensional (2D), the 3D tyre finite element model was obtained by rotating the 2D tyre model. To reduce the modelling workload, only half of the tyre profile was selected for modelling. The specific modelling process employed was as follows:

First, we drew a 2D profile of the tyre based on its size and material composition using AutoCAD and exported the *.iges file format to the HyperMesh 2021 pre-processing software for meshing. Considering that mesh quality has a major influence on the accuracy and convergence of the model results, the rubber material was divided into quadrilateral CGAX4 cells with triangular CGAX3 cells used only at the sharp corners of the material boundaries, and the cord skeleton material was represented by the SFMGAX1 cell type. In ABAQUS 2021, the material mechanical parameters were subsequently set based on the intrinsic tyre model, and a uniform pressure was applied to the inside of the tyre to simulate its inflation pressure. The resulting 2D tyre finite element model is shown in Figure 5.

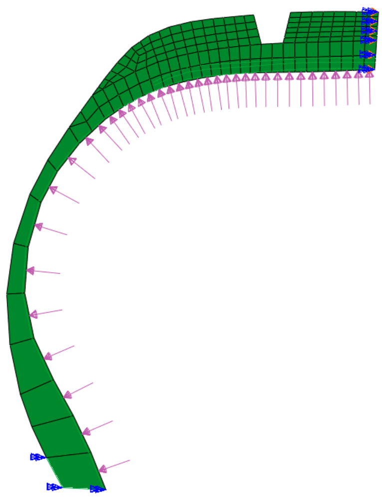

Figure 5. Two-dimensional finite element tyre model.

Second, the 2D finite element model of the tyre was rotated 360° around its rotation axis in ABAQUS 2021 to obtain half of the 3D finite element model, as shown in Figure 6. As the use of a dense tyre mesh can increase model calculation overhead but the use of a sparse tyre mesh can affect the accuracy of the results, mesh encryption was performed only in the contact interval between the tyre and pavement, and the mesh sizes of the tyre and pavement were matched to the greatest extent possible.

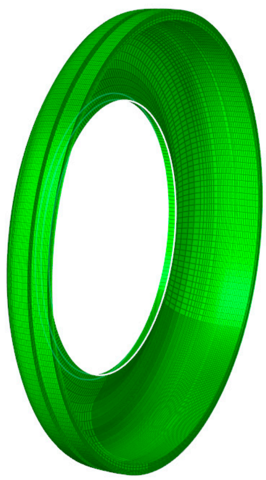

Figure 6. Half of the 3D finite element tyre model.

Third, half of the 3D finite element model was mirrored to obtain the completed 3D finite element model of the tyre, as shown in Figure 7. An analytical rigid body was used at the inner edge of the tyre bead to form the rim.

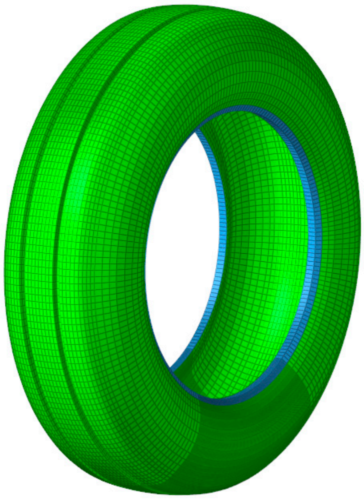

Figure 7. Complete 3D finite element tyre model.

3.2. Simplified Pavement Model

3.2.1. Simplified Pavement Consisting of a Single Grain Size Aggregate

Coarse aggregates larger than 4.75 mm can have a major impact on pavement skid resistance [27,28]; consequently, hemispherical shells with diameters of 7, 9, and 13 mm were used to represent different coarse aggregate grain sizes in three simplified pavements, each comprising a single grain size aggregate. The planar size of this simplified pavement was 200 × 200 mm, and the 7, 9, and 13 mm hemispherical shells were arranged in a matrix such that they numbered 28 × 28, 22 × 22, and 15 × 15, respectively. To ensure the convergence of the model and retain a sufficient pavement height, the heights of the simplified pavements with aggregate grain sizes of 7, 9, and 13 mm were set to 3, 4, and 5 mm, respectively. The 3D models of the simplified pavements were drawn using the CATIA V5R20 software, as shown in Figure 8.

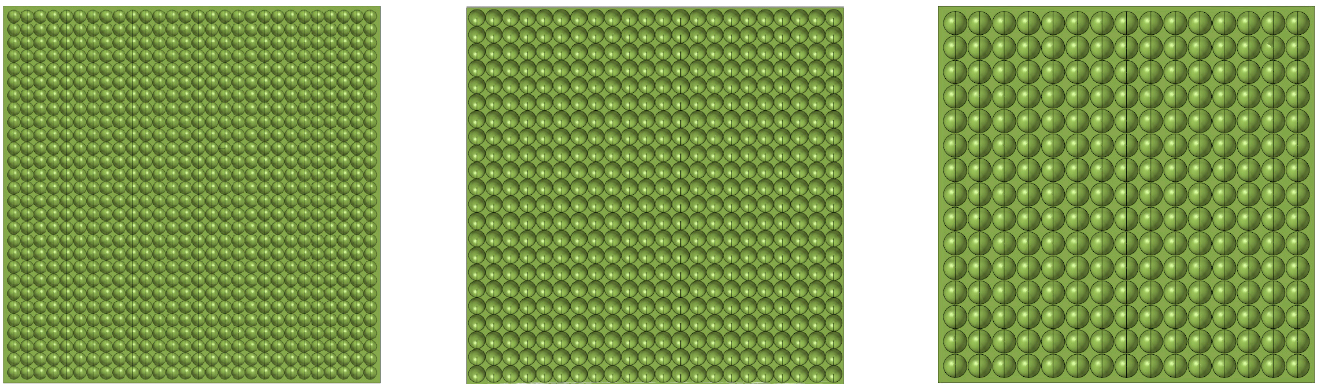

(**a**) (**b**) (**c**)

Figure 8. Three-dimensional model of simplified pavement. (**a**) Aggregate grain size 7 mm. (**b**) Aggregate grain size 9 mm. (**c**) Aggregate grain size 13 mm.

The pavement mean texture depth (*MTD*) was used to characterise the differences between the macrotextures of the simplified pavements and is expressed as follows:

$$MTD = \frac{V_1 - V_2}{A} \tag{3}$$

where V_1 denotes the cuboid volume within the height of the pavement bulge, V_2 denotes the volume of the pavement bulge, and A denotes the planar area of the pavement.

The pavement *MTD* values corresponding to aggregate grain sizes of 7, 9, and 13 mm were calculated using Equation (3); the results are shown in Table 3.

Table 3. Pavement mean texture depth (*MTD*) with aggregate grain sizes of 7, 9, and 13 mm.

Aggregate Grain Size	V_1 (mm^3)	V_2 (mm^3)	A (mm^2)	*MTD* (mm)
7 mm	120,000	55,417	40,000	1.61
9 mm	160,000	77,040	40,000	2.07
13 mm	200,000	85,412	40,000	2.86

3.2.2. Simplified Pavement Modelling

The primary objective of simplified pavement modelling is to divide the mesh of the pavement model. The simplified pavement model drawn using CATIA V5R20 was output in a saturated file format, then imported into HyperMesh 2021 for meshing. The pavement model was divided into quadrilateral cells to ensure mesh quality, as shown in Figure 9. Finally, the simplified pavement with sufficient meshing was output in the *.inp file format to import into ABAQUS 2021.

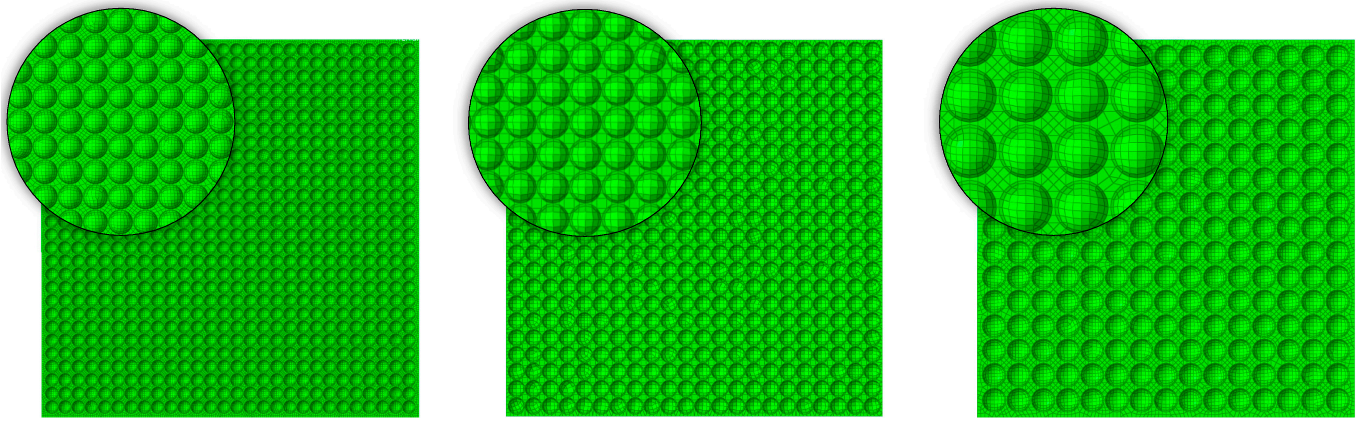

(**a**) (**b**) (**c**)

Figure 9. Three-dimensional mesh model of simplified pavement. (**a**) Aggregate grain size 7 mm. (**b**) Aggregate grain size 9 mm. (**c**) Aggregate grain size 13 mm.

3.3. *Tyre–Pavement Contact Model*

3.3.1. Contact and Boundary Settings

The stiffness of the simplified pavement model used in this study was considerably larger than that of the radial tyre model; consequently, the simplified pavement model could be regarded as a rigid body. The contact constraint of the tyre–pavement system was accordingly set to reflect the finite slip contact between rigid and deformed bodies in ABAQUS 2021. The tyre–pavement contact type was set to face-to-face contact, with the pavement set as the "master surface" and the tyre tread set as the "slave surface". For the contact property setting, the normal property was set as "hard contact", and the tangential property was set as the Coulomb friction model.

In ABAQUS 2021, the pavement was set to be stationary by constraints, and the travel speed of a tyre was simulated by setting the linear and angular velocities at the reference points of the rim. The tyre load was set in the negative direction of the Z-axis at the rim reference point. The 3D contact finite element model of the tyre and simplified pavement is shown in Figure 10.

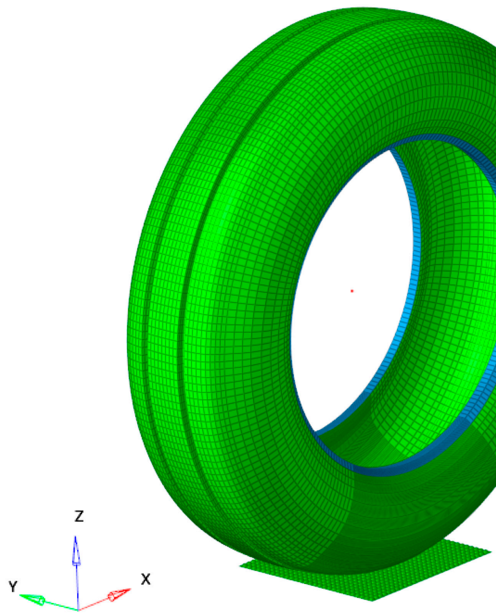

Figure 10. Three-dimensional contact model of the tyre and simplified pavement.

3.3.2. Contact Analysis

This study focused on the steady–state analysis of vehicle drive wheel and simplified pavement. Steady–state transport was used in ABAQUS 2021 to simulate the steady–state dynamic interaction between the tyre and rigid pavement surface. For this, the Eulerian description of rigid-body rotation and Lagrangian description of deformation were used to convert the steady–state moving contact problem into a purely spatially dependent simulation that described the rolling of the tyre as a material flow motion through the mesh.

To conduct a steady–state analysis, the motion state of the tyre can be set to steady–state rolling, braking, or driving. In ABAQUS 2021, the speed at which the tyre travels can be simulated in terms of linear and angular velocities, and the driving state of the tyre can be changed by transforming their combined values [29]; the relationship between the linear and angular velocities is given by

$$\omega = \frac{v}{r} \tag{4}$$

where ω denotes the angular velocity, v denotes the linear velocity, and r denotes the tyre radius of rotation. When the torque of the tyre around the rotation axis is zero, the tyre is in a stable rolling state; when the torque is non-zero, the tyre is accelerating or decelerating.

In the steady–state rolling analysis model, the tyre pressure was 260 kPa, the load was 2600 N, and the driving speed was 60 km/h, corresponding to a linear speed of 16.67 m/s. The angular velocity was initially calculated to be 57 rad/s based on the radius of the tyre. When simulated in ABAQUS 2021, the angular velocity was appropriately adjusted such that the tyre torque was close to zero. Eventually, the linear velocity was determined to be 16.67 m/s and the angular velocity 56.2 rad/s. Thus, when the linear velocity remained constant, tyres with angular velocities less than 56.2 rad/s were decelerating, whereas tyres with angular velocities greater than 56.2 rad/s were accelerating.

In the steady–state braking analysis model, the tyre pressure was 260 kPa, the load was 2600 N, the friction coefficient was 0.3, and the driving initial speeds were 30, 60, 90, and 120 km/h. Using the methods described in the previous paragraph, the linear and angular speeds of the tyres were determined for the different speeds during steady–state braking, and simulation analyses were performed using these values.

4. Results and Discussion

4.1. Steady–State Rolling Analysis

4.1.1. Contact Stress and Contact Area

To analyse the contact stress and contact area of the simplified pavement according to aggregate grain size, the 3D tyre–pavement contact model was used to simulate the steady–state rolling of a vehicle at a driving speed of 60 km/h, as shown in Figures 11 and 12.

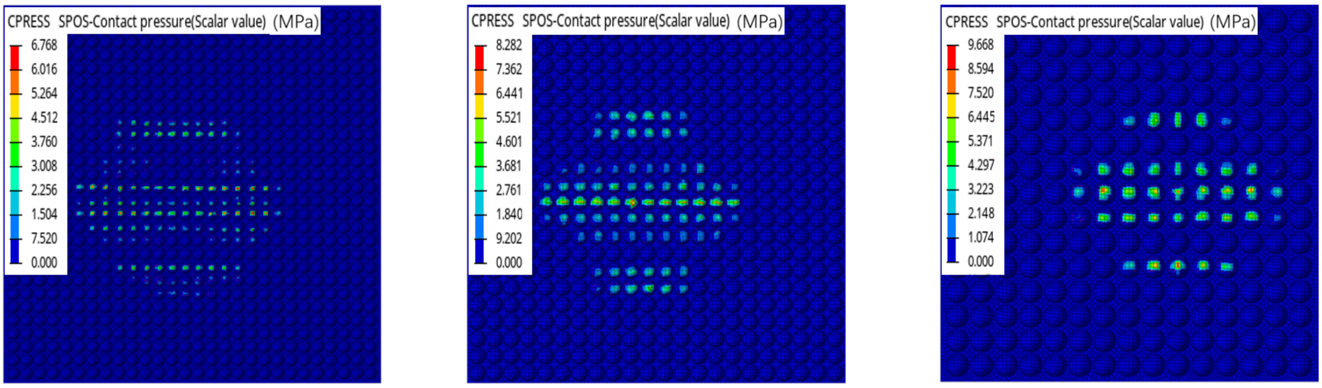

(**a**) (**b**) (**c**)

Figure 11. Contact stresses of simplified pavement during steady–state rolling. (**a**) Aggregate grain size 7 mm. (**b**) Aggregate grain size 9 mm. (**c**) Aggregate grain size 13 mm.

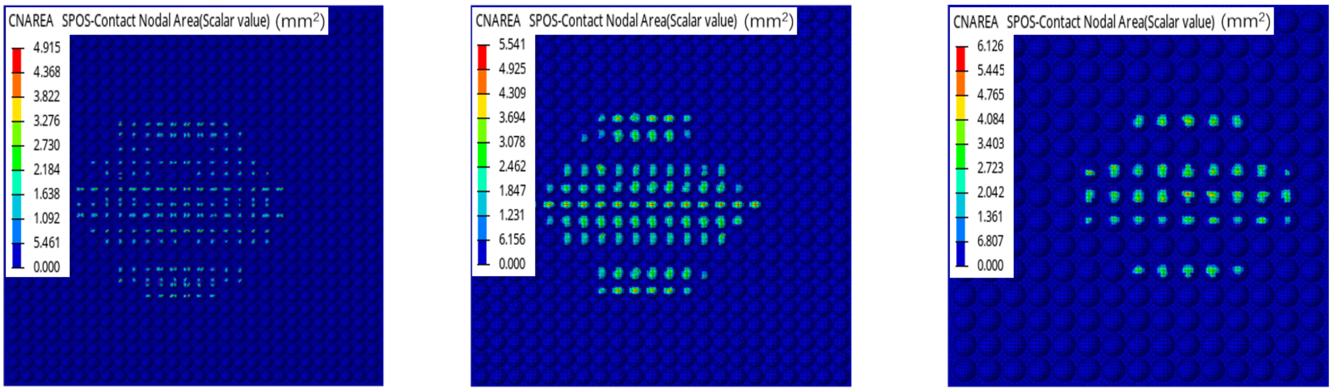

(**a**) (**b**) (**c**)

Figure 12. Contact areas of simplified pavements during steady–state rolling. (**a**) Aggregate grain size 7 mm. (**b**) Aggregate grain size 9 mm. (**c**) Aggregate grain size 13 mm.

As shown in Figure 11a–c, the general extent of contact stresses between the tire and each simplified pavement was similar; however, the different aggregate sizes resulted in different magnitudes of contact stress on each pavement. The peak stresses on the simplified pavements with aggregate grain sizes of 7, 9, and 13 mm were 6.77, 8.28, and 9.67 MPa, respectively. As shown in Table 3, the *MTD* values of the simplified pavements with aggregate grain sizes of 7, 9, and 13 mm were 1.61, 2.07, and 2.86 mm, respectively. These results show that both the *MTD* values and peak contact stresses on the simplified pavements were positively correlated with the aggregate grain size.

As shown in Figure 12a–c, the overall shape of the contact area between the tyre and each simplified pavement was similar; however, the size of the contact area decreased with the change in the macrotexture of the simplified pavement corresponding to the increase in aggregate grain size. To quantitatively simplify the contact area characterisation of the pavement according to aggregate grain size, we outputted the contact area of each simplified pavement in the software post-processing, as shown in Figure 13.

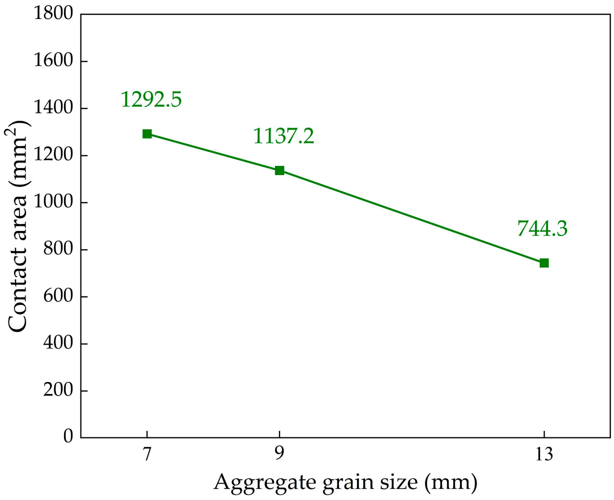

Figure 13. Contact area of each simplified pavement during steady–state rolling.

As shown in Figure 13, the maximum contact areas of simplified pavements with aggregate grain sizes of 7, 9, and 13 mm were 1292.5, 1137.2, and 744.3 mm^2, respectively. These results demonstrate that the contact area of the simplified pavement decreased as its aggregate grain size increased, indicating that pavements with large *MTD* values will have small contact areas.

4.1.2. Occlusal Depth

Based on the modelled contact area between the tyre and pavement, the nodal coordinates of the vertices and contact critical points of the aggregate were output using the post-processing module in ABAQUS 2021. The mean and cumulative occlusal depths of each simplified pavement model were subsequently calculated using Equations (1) and (2) with the results shown in Figures 14 and 15.

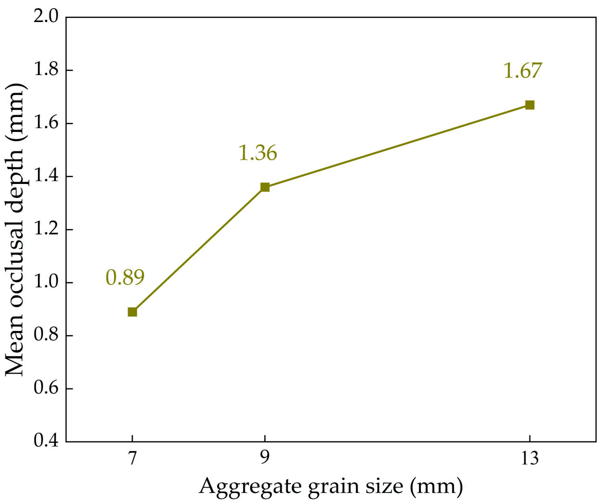

Figure 14. Mean occlusal depth of simplified pavement according to aggregate grain size.

As shown in Figures 14 and 15, the mean occlusal depths of the simplified pavements increased with increasing aggregate grain size, although the magnitude of the cumulative occlusal depth did not exhibit any correlation with aggregate grain size. As shown in Table 3, the *MTD* values of the simplified pavements with aggregate grain sizes of 7, 9, and 13 mm were 1.61, 2.07, and 2.86 mm, respectively. The results indicate that during the late stages of pavement skid resistance, a larger aggregate grain size will increase the *MTD* and mean occlusal depth of the pavement. However, the cumulative occlusal depth of a pavement with a larger aggregate grain size will be smaller because of the fewer points of contact between the pavement and tyre. As the cumulative occlusal depth of the pavement directly reflects the overall deformation of the tyre tread, under tyre rolling conditions, pavement with a smaller aggregate grain size will increase the overall deformation of the tyre tread, thereby producing better contact interaction.

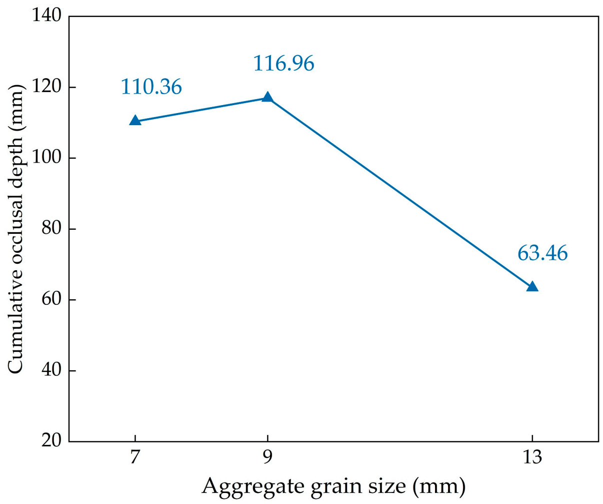

Figure 15. Cumulative occlusal depth of simplified pavement according to aggregate grain size.

4.2. Steady–State Braking Analysis

The effect of the contact interaction between the tyre and simplified pavements with different aggregate grain sizes can be further analysed in terms of the horizontal braking force. In this study, the steady–state braking of a vehicle travelling at initial speeds of 30, 60, 90, and 120 km/h was simulated using the established 3D tyre–pavement contact finite element model. After simulation, the horizontal combined force of the contact force and friction force is output in the post-processing of the software, which is the horizontal braking force, as shown in Figure 16. The cumulative occlusal depth of each simplified pavement for vehicles traveling at different speeds was calculated using Equations (1) and (2), as shown in Figure 17. To verify that the cumulative occlusal depth accurately reflected the contact interaction between the tyre and pavement aggregate, an analysis of the correlation between the cumulative occlusal depth and horizontal braking force of the simplified pavement was conducted, with the results shown in Figure 18.

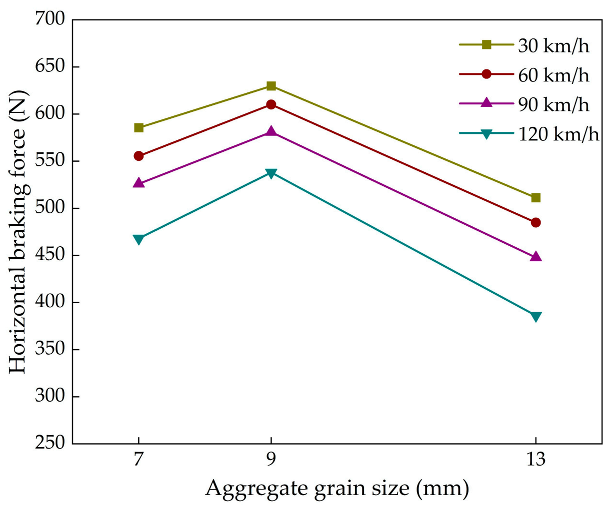

Figure 16. Horizontal braking force of each simplified pavement at different vehicle initial speeds.

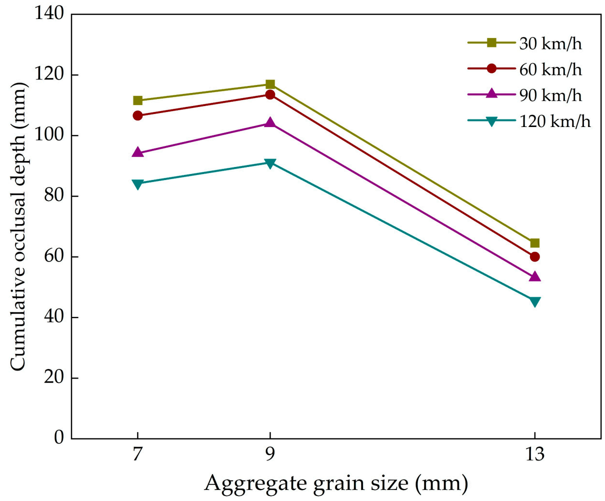

Figure 17. Cumulative occlusal depth of each simplified pavement at different vehicle initial speeds.

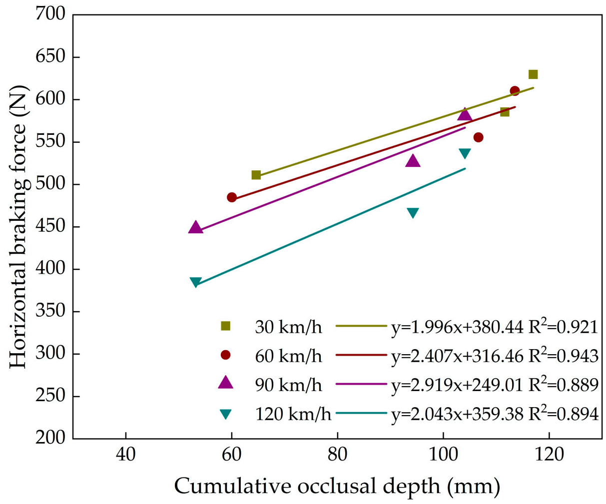

Figure 18. Correlation analysis between horizontal braking force and cumulative occlusal depth.

As shown in Figures 16 and 17, the horizontal braking force and cumulative occlusal depth for each simplified pavement decreased as the vehicle speed increased, with both the horizontal braking force and cumulative occlusal depth for the simplified pavements ranked from largest to smallest as aggregate grain sizes 9, 7, and 13 mm at all four speeds. As shown in Table 3, the *MTD* values of the simplified pavements with aggregate grain sizes of 7, 9, and 13 mm were 1.61, 2.07, and 2.86 mm, respectively. Thus, the effect of the contact interaction between the tyre and simplified pavement aggregates was ranked in order of superiority as aggregate grain sizes of 9, 7, and 13 mm, indicating that the aggregate grain size does not exhibit any correlation with tyre–pavement contact interaction in the later stages of pavement skid resistance. Though the increase in aggregate grain size resulted in a larger *MTD* of the simplified pavement, this does not indicate a better contact interaction effect between the tyre and pavement.

As shown in Figure 18, the squares of linear correlation coefficients between the horizontal braking force and pavement cumulative occlusal depth were 0.921, 0.941, 0.889, and 0.894 for vehicle initial speeds of 30, 60, 90, and 120 km/h, respectively, indicating that using the pavement cumulative occlusal depth to characterise the effect of contact interaction between the tyre and pavement aggregate is accurate and can be used to evaluate asphalt pavement skid resistance.

5. Conclusions

This study considered three simplified pavements comprising aggregates of different grain sizes as the research object to develop a 3D finite element tyre–pavement contact model in ABAQUS 2021. First, the contact stress and contact area distribution characteristics of each simplified pavement and the occlusal depth of the tyre–pavement system were analysed under steady–state rolling conditions. Subsequently, the horizontal braking force and cumulative occlusal depth of each simplified pavement were analysed at different vehicle speeds under steady–state braking conditions, and a correlation analysis between these parameters was conducted. The results of this study can be summarised as follows:

1. Under steady–state rolling conditions, the overall shape of the contact area between the tyre and each simplified pavement was similar; however, the peak contact stresses on the simplified pavement increased with its *MTD*, whereas pavements with larger *MTD* values exhibited smaller contact areas.
2. Under steady–state rolling conditions, the mean occlusal depth of the simplified pavement was positively correlated with the aggregate grain size. However, the cumulative occlusal depth did not exhibit any correlation with the aggregate grain size and ranked from largest to smallest as aggregate grain sizes 9, 7, and 13 mm. These results indicate that a simplified pavement with a smaller aggregate grain size exhibited a larger overall deformation of the tyre tread, implying that the grain size of the pavement aggregate bulge affects pavement skid resistance during the later stages.
3. Under steady–state braking conditions, the effect of the contact interaction between the tyre and simplified pavement aggregates was ranked in order of superiority as aggregate grain sizes of 9, 7, and 13 mm, indicating that during the late stages of pavement skid resistance, the two smaller aggregates provided superior performance. Consequently, to ensure the durability of pavement skid resistance, more consideration should be given to aggregates with grain sizes in the 7–9 mm range during pavement design.
4. The squares of linear correlation coefficients between the horizontal braking force and pavement cumulative occlusal depth were 0.921, 0.941, 0.889, and 0.894 for vehicle speeds of 30, 60, 90, and 120 km/h, respectively, indicating that the cumulative occlusal depth can be confidently used for the assessment of pavement skid resistance.

Note that this study was limited to the use of specific tyre and simplified pavement models. In future research, experimental studies will be conducted on pavements with actual aggregate compositions using different types of tyres. These limitations notwithstanding, the conclusions of this study indicate a clear direction for application and can contribute to the development of skid resistance design methods for asphalt pavements.

Author Contributions: Conceptualization, Z.L. and W.C.; methodology, Z.L.; software, W.C.; validation, W.W., Z.L. and Y.L.; formal analysis, W.C.; investigation, Y.L.; resources, W.W.; data curation, Y.L.; writing—original draft preparation, W.C.; writing—review and editing, Z.L.; visualization, Y.L.; supervision, W.W.; project administration, W.W.; funding acquisition, Z.L. All authors have read and agreed to the published version of the manuscript.

Funding: This study received no external funding.

Data Availability Statement: The data presented in this study are available on request from the corresponding author. The data are not publicly available due to privacy.

Conflicts of Interest: The authors declare no conflict of interest.

References

1. Rasol, M.; Schmidt, F.; Ientile, S.; Adelaide, L.; Nedjar, B.; Kane, M.; Chevalier, C. Progress and Monitoring Opportunities of Skid Resistance in Road Transport: A Critical Review and Road Sensors. *Remote Sens.* **2021**, *13*, 3729. [CrossRef]
2. Fang, T.; Guo, R.; Si, Y. Ensemble Mode and Singular Value Based Road Texture-Skid Study. *Coatings* **2021**, *11*, 947. [CrossRef]
3. Wang, H.; Liu, Y.; Yang, J.; Shi, X.; Xu, X.; Luo, S.; Huang, W. Evaluation of Anti-Skid Performance of Asphalt Mixture Based on Accelerated Loading Test. *Appl. Sci.* **2023**, *13*, 4796. [CrossRef]

4. Sabri, M.; Abda, S. Grip Analysis of Road Surface and Tire Footprint Using FEM. In Proceedings of the 10th International Conference Numerical Analysis in Engineering (NAE), Banda Aceh, Indonesia, 24–25 August 2018; IOP: Bristol, UK, 2018; Volume 308, p. 012018.
5. Huang, W.; Liu, C.; Guo, W.; Wei, Y. A Surface Texture Prediction Model Based on RIOHTrack Asphalt Pavement Testing Data. *Appl. Sci.* **2022**, *12*, 10539. [CrossRef]
6. Dong, Y.; Wang, Z.; Ren, W.; Jiang, T.; Hou, Y.; Zhang, Y. Influence of Morphological Characteristics of Coarse Aggregates on Skid Resistance of Asphalt Pavement. *Materials* **2023**, *16*, 4926. [CrossRef] [PubMed]
7. Zhang, Y.; Allen, A.W.; Yi, J.; Liu, T. Understanding Tire/Road Stick-Slip Interactions with Embedded Rubber Force Sensors. In Proceedings of the IEEE/ASME International Conference on Advanced Intelligent Mechatronics (AIM), Kaohsiung, Taiwan, 11–14 July 2012; IEEE: Washington, DC, USA, 2012; pp. 550–555.
8. Zhang, Y.; Yi, J. Static Tire/Road Stick–Slip Interactions: Analysis and Experiments. *IEEE/ASME Trans. Mechatron.* **2013**, *19*, 1940–1950. [CrossRef]
9. Chen, B.; Zhang, X.; Yu, J.; Wang, Y. Impact of contact stress distribution on skid resistance of asphalt pavements. *Constr. Build. Mater.* **2017**, *133*, 330–339. [CrossRef]
10. Liu, X.; Al-Qadi, I.L. Three-dimensional tire-pavement contact stresses prediction by deep learning approach. *Int. J. Pavement Eng.* **2022**, *23*, 4991–5002. [CrossRef]
11. Liu, X.; Jayme, A.; Al-Qadi, I.L. ContactGAN development-prediction of tire-pavement contact stresses using a generative and transfer learning model. *Int. J. Pavement Eng.* 2022, 1–11, *ahead-of-print*. [CrossRef]
12. Xie, Y.; Yang, Q. Tyre–pavement contact stress distribution considering tyre types. *Road Mater. Pavement Des.* **2019**, *20*, 1899–1911. [CrossRef]
13. He, H.; Li, R.; Yang, Q.; Pei, J.; Guo, F. Analysis of the Tire-Pavement Contact Stress Characteristics during Vehicle Maneuvering. *KSCE J. Civil Eng.* **2021**, *25*, 2451–2463. [CrossRef]
14. Tang, X.; Xie, J.; Xie, H.; Zhang, H. Predictions of three-dimensional contact stresses of a radial truck tire under different driving modes. *Adv. Mech. Eng.* **2022**, *14*, 1992380011. [CrossRef]
15. Lin, C.; Wang, T. Effect of fine aggregate angularity on skid-resistance of asphalt pavement using accelerated pavement testing. *Constr. Build. Mater.* **2018**, *168*, 41–46. [CrossRef]
16. Xiao, S.-Q.; Tan, Y.-Q.; Xing, C.; Zhou, X.-L. Scale demarcation of self-affine surface of coarse aggregate and its relationship with rubber friction. *Road Mater. Pavement Des.* **2021**, *22*, 1842–1859. [CrossRef]
17. Riahi, E.; Do, M.-T.; Kane, M. An energetic approach to model the relationship between tire rolling friction and road surface macrotexture. *Surf. Topogr. Metrol. Prop.* **2022**, *10*, 014001. [CrossRef]
18. Yu, M.; Kong, Y.; Wu, C.; Xu, X.; Li, S.; Chen, H.; Kong, L. The Effect of Pavement Texture on the Performance of Skid Resistance of Asphalt Pavement Based on the Hilbert-Huang Transform. *Arab. J. Sci. Eng.* **2021**, *46*, 11459–11470. [CrossRef]
19. Sharma, A.K.; Bouteldja, M.; Cerezo, V. Multi-physical model for tyre–road contact—The effect of surface texture. *Int. J. Pavement Eng.* **2022**, *23*, 755–772. [CrossRef]
20. Persson, B.N.J. Theory of rubber friction and contact mechanics. *J. Chem. Phys.* **2001**, *115*, 3840–3861. [CrossRef]
21. Lorenz, B.; Persson, B.N.J.; Dieluweit, S.; Tada, T. Rubber friction: Comparison of theory with experiment. *Eur. Phys. J. E* **2011**, *34*, 129. [CrossRef]
22. Heinrich, G.; Klueppel, M. Rubber friction, tread deformation and tire traction. *Wear* **2008**, *265*, 1052–1060. [CrossRef]
23. Lorenz, B.; Oh, Y.R.; Nam, S.K.; Jeon, S.H.; Persson, B.N.J. Rubber friction on road surfaces: Experiment and theory for low sliding speeds. *J. Chem. Phys.* **2015**, *142*, 194701. [CrossRef]
24. Wang, H.; Wang, Z. Evaluation of pavement surface friction subject to various pavement preservation treatments. *Constr. Build. Mater.* **2013**, *48*, 194–202. [CrossRef]
25. Yu, M.; Wu, G.; Kong, L.; Tang, Y. Tire-Pavement Friction Characteristics with Elastic Properties of Asphalt Pavements. *Appl. Sci.* **2017**, *7*, 1123. [CrossRef]
26. Zong, Y.; Xiong, R.; Wang, Z.; Zhang, B.; Tian, Y.; Sheng, Y.; Xie, C.; Wang, H.; Yan, X. Effect of morphology characteristics on the polishing resistance of coarse aggregates on asphalt pavement. *Constr. Build. Mater.* **2022**, *341*, 127755. [CrossRef]
27. Uz, V.E.; Gokalp, I. The effect of aggregate type, size and polishing levels to skid resistance of chip seals. *Mater. Struct.* **2017**, *50*, 126. [CrossRef]
28. Wasilewska, M.; Gierasimiuk, P.; Gardziejczyk, W. Comparison of skid resistance of EAC pavement with different maximum aggregate grain size. *Int. J. Pavement Eng.* **2022**, *23*, 3930–3940. [CrossRef]
29. Yu, L.; Hu, J.; Li, R.; Yang, Q.; Guo, F.; Pei, J. Tire-Pavement Contact Pressure Distribution Analysis Based on ABAQUS Simulation. *Arab. J. Sci. Eng.* **2022**, *47*, 4119–4132. [CrossRef]